HTML ABSTRACT + LINKS

Real-time observation of initial stages of copper film growth on silicon oxide using reflection high-energy electron diffraction

Jason T. Drotar,[a] T.-M. Lu, and G.-C. Wang
Department of Physics, Applied Physics, and Astronomy, Rensselaer Polytechnic Institute, 110 8th Street, Troy, New York 12180-3590

(Received 21 June 2004; accepted 8 September 2004)

We have studied, in real time, the evolution of a thin (less than 200 Å) copper film deposited onto an oxidized silicon surface using reflection high-energy electron diffraction. We show that quantitative measurements of island size and shape as functions of time are possible and the results are presented. While the film texture is initially random, texture competition leads to an absence of the low-energy (111) and (200) oriented grains for later times. It is also found that the film surface is composed of facets that increase in size with time. This behavior is explained in terms of facet coalescence. © *2004 American Institute of Physics*. [DOI: 10.1063/1.1811785]

I. INTRODUCTION

Due to its low resistivity, copper is a technologically important material. Studies of copper deposition onto clean silicon surfaces have revealed that copper and silicon interact strongly, forming copper silicide in some cases.[1–5] To prevent silicide formation, two different strategies can be employed. First, silicon can be passivated by Hartree-Fock (HF) dipping. This etches away the native oxide and results in a hydrogen-terminated surface. Another strategy is to deposit the copper film on the native oxide of silicon. Both strategies prevent silicide formation, provided the temperature remains low enough.

While the deposition of copper on hydrogen-terminated silicon[6–10] and silicon oxide[10–14] substrates has been studied, none of these studies have examined, in detail, the temporal behavior of such processes. In the present study, thin copper films were thermally evaporated onto the native oxide of Si(111). Using reflection high-energy electron diffraction (RHEED), the structural evolution was monitored in real time, and the results are compared with existing models of polycrystalline film growth.

II. EXPERIMENT

The experiments were conducted in an ultrahigh vacuum chamber with a base pressure of 4×10^{-10} Torr or better, and the evaporated films were examined using Auger electron spectroscopy and RHEED. The RHEED images were acquired by imaging a phosphor screen using a charge-coupled device (CCD) camera.

A. Sample preparation

The samples used were cut from a phosphorous-doped (1–5 Ω cm) Si(111) wafer and were cleaned for 5 min in acetone using an ultrasonic cleaner. It is well known that silicon forms a thin native oxide in air. Grundner and Jacob found that Si(100) forms an oxide layer at the surface ≈15 Å thick,[15] and the same type of behavior is expected for Si(111). The sample used in the real-time deposition was also subjected to the first stage of RCA cleaning.[16] An Auger spectrum for the clean surface is shown in Fig. 1. For silicon oxide, peaks are expected at 90 and 503 eV.[17] As expected, peaks are observed near these locations. However, a third peak, near 271 eV, is also observed due to carbon contamination.

To determine the structure of the RCA-cleaned surface, RHEED patterns were acquired for three different angles of incidence. The primary energy, in each case, is 8 keV, and the angles of incidence are 0.53°, 0.63°, and 0.69° with respect to the surface. One such image is shown in Fig. 2. The bright spot on the left side of the image is simply the portion of the electron beam that has missed the sample. To the right of this spot is the shadow edge. The shadow edge is the boundary between the region where there is no diffraction intensity and the region where there is some diffraction intensity; the area to the left of the shadow edge is dark (aside from the aforementioned spot), while the area to the right of the shadow edge is much brighter, due to the diffracted electrons. To the right of the shadow edge is a single diffraction spot, which is caused by reflection of the electron beam from

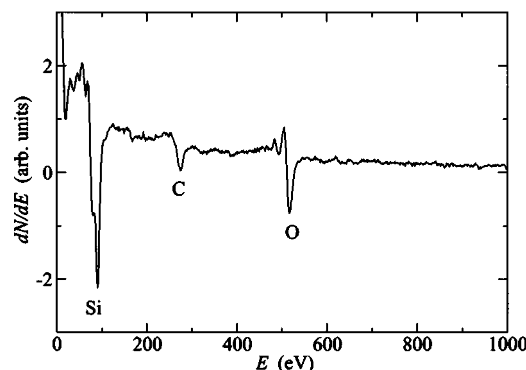

FIG. 1. A derivative Auger spectrum for the RCA-cleaned Si(111) surface. Peaks are observed near the expected locations of 90 and 503 eV. The remaining peak is due to the presence of carbon.

[a]Present address: Code G22, Naval Surface Warfare Center, Dahlgren Division, 17320 Dahlgren Road, Dahlgren, VA 22448; electronic mail: drotarj@nswc.navy.mil

0021-8979/2004/96(12)/7071/9/$22.00 © 2004 American Institute of Physics

Downloaded 21 Apr 2006 to 128.113.7.25. Redistribution subject to AIP license or copyright, see http://jap.aip.org/jap/copyright.jsp

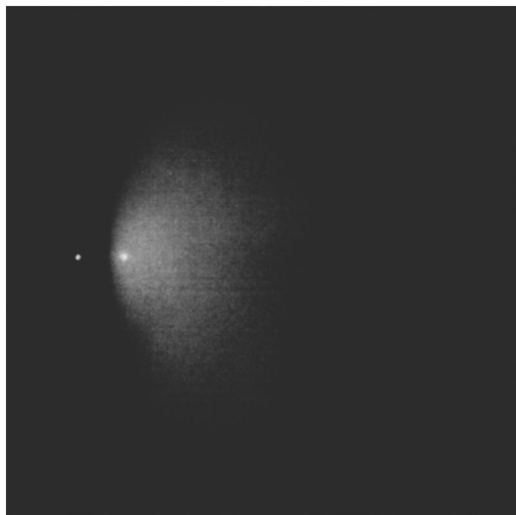

FIG. 2. A RHEED image for the RCA-cleaned Si(111) surface. The grayscale indicates the electron intensity; black indicates low intensity, while white indicates high intensity. A single spot is seen to the right of the shadow edge. The primary energy is 8 keV and the angle of incidence is ≈0.63° from the surface.

the surface of the sample. This spot is referred to as the specular spot, and it contains information on the surface structure of the sample. The rest of the diffraction pattern consists of diffuse scattering, which is due to the atomic structure of the sample; the lack of rings or additional spots indicates that the sample is amorphous, at least near the surface.

By looking at the variation of the diffraction intensity with the momentum transfer $\vec{K}$, it is possible to deduce certain properties of the sample surface. For a continuous Gaussian surface, the diffraction intensity follows[18]

$$I(\vec{K}) \propto 4\pi^2 e^{-(K_\perp w)^2} \delta(\vec{K}_\parallel) + I_{\mathrm{diffuse}}(\vec{K}_\parallel, \vec{K}_\perp), \tag{1}$$

where w is the interface width of the surface, $\vec{K}_\parallel$ is the component of $\vec{K}$ parallel to the surface, $K_\perp$ is the component of $\vec{K}$ perpendicular to the surface, and I_{diffuse} is given by[18]

$$I_{\mathrm{diffuse}} = \int \left(e^{-(1/2)K_\perp^2 H(\vec{r})} - e^{-(K_\perp w)^2}\right) e^{i\vec{K}_\parallel \cdot \vec{r}} d^2 r. \tag{2}$$

Equations (1) and (2) will be true, regardless of the surface height distribution, if $(k_\perp w)^2 \ll 1$.[19] By making use of Eq. (1), it is possible to determine the interface width w of the sample surface. In Fig. 3, $\ln(I)$ is plotted versus $K_\perp^2$, where I is the maximum intensity of the specular spot above the diffuse background. According to Eq. (1), this plot should give a straight line with a slope of $-w^2$. From the plot, it was found that $w = 2.03 \pm 0.13$ Å, where the error was determined using normal regression analysis. This value of w is consistent with that obtained by atomic force microscopy.

B. Deposition source

The copper films were deposited using thermal evaporation. The concept of thermal evaporation is relatively simple; when an elemental substance is heated to near its melting point, the atoms of the substance will evaporate from the surface. The deposition source design used in this study is shown in Fig. 4. A piece of 0.25 mm thick copper foil of 99.9999% purity is heated using a combination of electron bombardment and radiative heating. A filament composed of 0.25 mm tungsten wire is heated resistively using a current of 5.5 A. Since the filament is only about 1.5 mm from the copper foil, the copper foil is heated by radiation from the filament. The foil can also be heated by electron bombardment; by biasing the filament at a negative voltage with respect to the copper foil, electrons can be extracted from the hot filament. The electron current extracted from the filament is referred to as the emission current, and its magnitude depends on both the filament current and the bias voltage. The extracted electrons are accelerated towards the foil by the potential difference between the filament and foil and eventually collide with the foil.

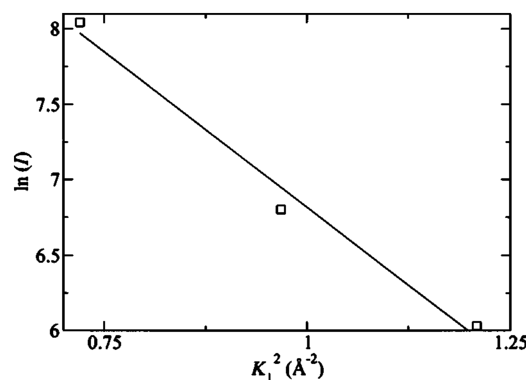

FIG. 3. $\ln(I)$ plotted vs $K_\perp^2$. The straight line is a least-squares fit of the data. From the slope of the line, it was found that $w = 2.03 \pm 0.13$ Å. The error was computed using normal regression analysis.

There are many special considerations to take into account when designing a deposition source that is suitable for real-time deposition studies. For the design used in this study, the filament is surrounded by a tantalum shield. The shield serves three purposes. First, it helps trap heat within the source. This lowers the filament current needed to achieve a given deposition rate, and it also prevents the source from heating the surrounding environment. The shield also blocks light from the filament. Even with the shield, a considerable amount of light still reaches the phosphor screen. The light that makes it through the phosphor screen will be detected by the CCD camera and will appear as an additional background in the diffraction pattern. While this background can be subtracted, it will still add a considerable amount of noise to the diffraction pattern. The final purpose of the shield is to shield the rest of the chamber from the

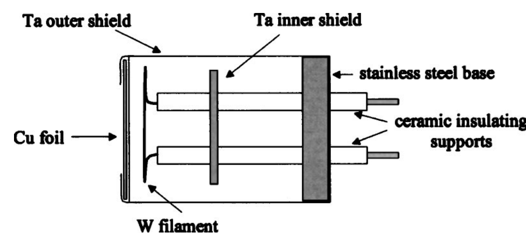

FIG. 4. A top view of the deposition source used for real-time copper deposition.

Downloaded 21 Apr 2006 to 128.113.7.25. Redistribution subject to AIP license or copyright, see http://jap.aip.org/jap/copyright.jsp

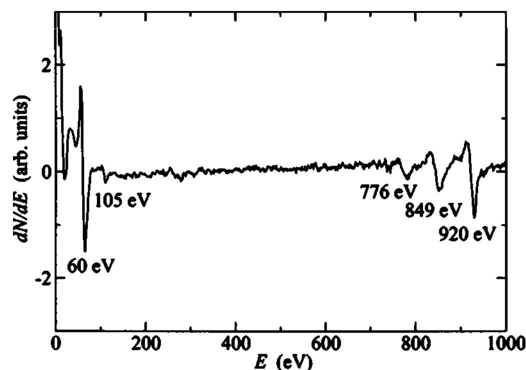

FIG. 5. A derivative Auger spectrum for copper deposited on the native oxide of Si(111). The total deposition time is 28 min. Peaks are observed near the expected locations of 60, 105, 776, 849, and 920 eV. The beam energy is 3 keV.

filament bias voltage; the shield is grounded, which prevents stray electric fields from deflecting or distorting the electron beam used in the RHEED measurements. Since the copper foil is held by the outer tantalum shield, it is also grounded. Therefore the filament must be biased at a negative voltage with respect to ground. In such a situation, the extracted electrons would be attracted to both the foil and shield. To prevent bombardment of the outer shield, an inner tantalum shield is placed behind the filament. This inner shield is biased at the same voltage as the filament.

In the present study, the copper deposition was carried out using a filament current of 5.5 A and a bias voltage of 150 V. These conditions result in a filament emission current of $\approx$90 mA, which gives a total bombardment power of 13.5 W. The sample was not deliberately heated, but due to its proximity to the deposition source, it reached a temperature of about 120 °C. This was determined by measuring the temperature, with a thermocouple, for a separate sample. The source conditions for this sample were similar to the conditions of the experiment. The temperature rose to 100 °C within 20 min, but never rose above 120 °C. The deposition flux is normally incident upon the sample from a distance of about 5 cm, and to determine the deposition rate interrupted depositions were performed up to a total deposition time of 28 min. An Auger spectrum for the 28 min film is shown in Fig. 5. The spectrum shows no trace of silicon (90 eV) or oxygen (503 eV), and the amount of carbon contamination (271 eV) is almost negligible. Auger spectra were also acquired for the shorter-time depositions. By looking at the ratio of the 60 and 920 eV peaks, it was possible to determine the deposition rate using the equation

$$\frac{I_{60}}{I_{920}} \propto \frac{(1-e^{-t/(\lambda_{60}\cos\phi)})}{(1-e^{-t/(\lambda_{920}\cos\phi)})}, \tag{3}$$

where λ_{60} is the attenuation constant of the Auger electrons in copper at 60 eV, λ_{920} is the attenuation constant of the Auger electrons in copper at 920 eV, t is the film thickness, and ϕ is the accepting angle of the Auger electron spectrometer. The attenuation constants were found by using the empirical formula of Seah and Dench[20] and the deposition rate was found to be $\approx 1.0\pm 0.5$ Å/min, where the error is a consequence of the uncertainty in the attenuation factors.

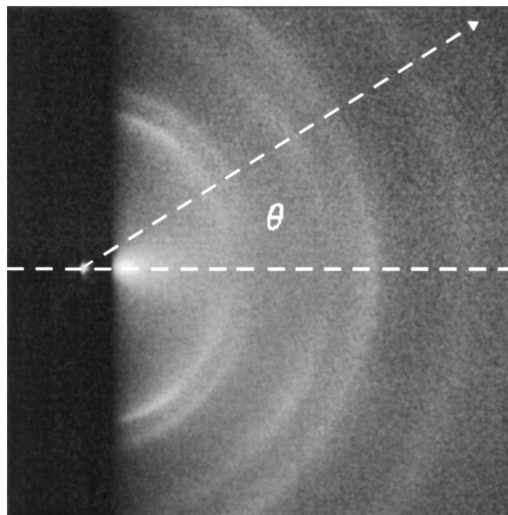

FIG. 6. The final RHEED image for the 170 min real-time copper deposition. The primary energy is 8 keV and the angle of incidence is $\approx$0.77° from the surface.

III. RESULTS

To determine the temporal dependence of the film structure, a continuous deposition of copper was performed, and the structure was monitored in real time using RHEED. Since the source conditions used in the real-time deposition are almost identical to the conditions used in the interrupted depositions, it is assumed that the deposition rate is the same in both cases. The total deposition time is 170 min, and one RHEED image was acquired every minute during the deposition, resulting in 170 images. The final RHEED image, acquired after 170 min of deposition, is shown in Fig. 6. There are two obvious features in this image. First, the image contains five concentric (and in some cases, broken) rings. These rings are a consequence of the crystal structure of the film. The second feature in the RHEED image is the appearance of a specular reflection near the shadow edge. This specular reflection contains information on the surface of the film. Note that the angle θ is used to specify positions along rings.

The existence of rings in the RHEED image implies that the copper film is polycrystalline. In other words, the film comprises many small crystals. For copper, it is expected that the individual crystals have a face-centered cubic (fcc) structure. For fcc lattices, one generally starts from a cubic lattice with primitive lattice vectors $\vec{r}_x=(a,0,0)$, $\vec{r}_y=(0,a,0)$, and $\vec{r}_z=(0,0,a)$, where a is the cubic lattice constant. To obtain a fcc lattice, one adds four basis atoms for each point in the cubic lattice. The basis atoms are at (0,0,0), $[(a/2),(a/2),0]$, $[0,(a/2),(a/2)]$, and $[(a/2),0,(a/2)]$ with respect to the given cubic lattice point. The reciprocal lattice vectors are $\vec{k}_x=[(2\pi/a),0,0]$, $\vec{k}_y=[0,(2\pi/a),0]$, and $\vec{k}_z=[0,0,(2\pi/a)]$. Because of the basis atoms, reciprocal lattice points denoted by indices (hkl) vanish unless h, k, and l are either all even or all odd. If the copper film were a single crystal, the RHEED image would comprise many spots. However, the film is actually made up of many small crystals of various orientations, and it is assumed that the diffraction amplitudes from different crystals have a random phase relationship. In

Downloaded 21 Apr 2006 to 128.113.7.25. Redistribution subject to AIP license or copyright, see http://jap.aip.org/jap/copyright.jsp

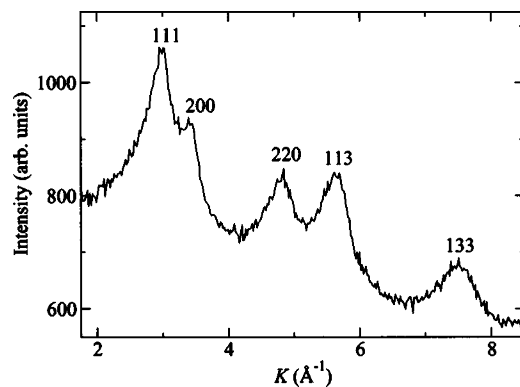

FIG. 7. Radially averaged intensity for the 170 min RHEED image.

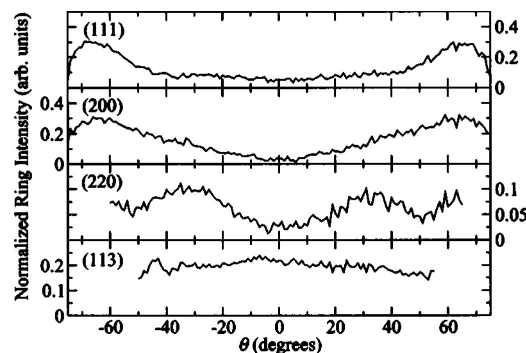

FIG. 8. Normalized ring intensity vs θ averaged over the last ten (161–170 min) images, for the first four rings.

such a situation, the diffraction intensity is merely the sum of diffraction intensities from all of the individual crystals. For an individual crystal, the diffraction pattern is made up of a lattice of points whose orientation depends on the orientation of the crystal. While the actual positions of the reciprocal lattice points depend on the crystal orientation, their distance from the origin does not. If the crystal orientations are completely random, then for each diffraction spot, there is a corresponding sphere in reciprocal space. In a RHEED image, these spheres would appear as rings. For a reciprocal lattice point with indices (hkl), the corresponding sphere appears at

$$K^2 = (h^2 + k^2 + l^2)\frac{4\pi^2}{a^2}, \tag{4}$$

where K is the magnitude of $\vec{K}$.

In Fig. 7, the diffraction intensity is plotted as a function of K. This plot was obtained by averaging the diffraction intensity along an arc with the same center as the rings, for each value of r (in increments of 1 pixel), where r is the distance of the arc, in pixels, from the center of the rings. The angular range of the arc extends from $\theta = -65°$ to $\theta = +65°$. Note that, in the RHEED geometry, K is approximately proportional to r. The plot shows a peak for each ring. From the ring radii, it is possible to determine the lattice constant for the film and check whether or not the rings are consistent with diffraction from a fcc lattice. Using the first ring, the lattice constant is found to be 3.63 Å, which is very close to the expected value, for copper, of 3.61 Å. Using this value, the expected ring radii, for the remaining rings, can be computed. In Table I, the expected radii K_e are listed, along with the measured radii K_m. Note that the (222) and (400) rings are not observed. There are many possible reasons for this; these rings could be obscured by the diffuse diffraction intensity, but it is more likely that these rings simply have breaks in them, as is the case for the (111) and (200) rings. Since the range of data in the RHEED image is restricted, the unbroken parts of the (222) and (400) rings cannot be observed.

TABLE I. Measured and expected ring radii (K_m and K_e, respectively) for the 170 min RHEED image. The expected radii are computed using a latticed constant of 3.63 Å.

(hkl)	K_e (Å^{-1})	K_m (Å^{-1})	Percent error (%)
(111)	3.00	3.00	0.0
(200)	3.46	3.44	0.6
(220)	4.90	4.86	0.8
(113)	5.74	5.67	1.2
(222)	6.00	⋯	⋯
(400)	6.92	⋯	⋯
(133)	7.54	7.52	0.3

The observed diffraction rings also contain information on the orientation of the individual grains. This aspect of crystal structure is known as texture. If the grain orientations were completely random, then the rings would be uniform in intensity. The fact that some of the rings have breaks in them implies that there is at least some preferential alignment of grains. When looking at the ring intensity, one typically normalizes the intensity with respect to the diffuse background. First, the background intensity is subtracted from the intensity on the ring. Next, the ring intensity, after background subtraction, is divided by the background intensity. This last step is necessary, because the diffraction intensity is attenuated, due to multiple scattering effects, by an amount that depends on the distance from the shadow edge. The background, for a given point on a ring, is taken to be the diffraction intensity slightly to the outside of the ring on the line from the point to the center of the rings. In Fig. 8, the normalized ring intensity is shown as a function of θ for the first four rings. To reduce noise, the intensity profiles for the last ten RHEED images (from 161 to 170 min) were averaged. To properly characterize the sample texture, one should acquire RHEED images at several different in-plane sample orientations. This is clearly impractical for real-time sample characterization. Fortunately, though, it is unnecessary in the present study, because the deposition is at normal incidence. In such a case, the film is expected to be isotropic, and the RHEED images should be the same for any in-plane rotation. By convention, a grain is said to be oriented in the (hkl) direction if the (hkl) reciprocal lattice vector points in the direction perpendicular to the substrate. From the plot, there is a clear absence of (111), (200), and (220) oriented grains, and there is a slight abundance of (113) grains.

A. Temporal evolution of film structure

In Fig. 9, RHEED images, for the real-time deposition, are shown for various times. By looking at the rings, one can observe the development of texture in the film. For early

Downloaded 21 Apr 2006 to 128.113.7.25. Redistribution subject to AIP license or copyright, see http://jap.aip.org/jap/copyright.jsp

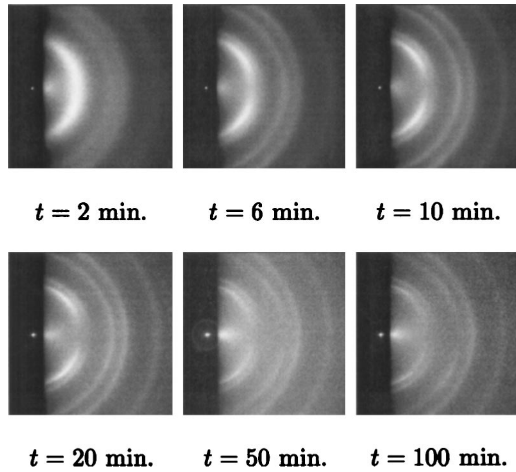

FIG. 9. RHEED images for the real-time copper deposition at various times.

times, the rings are nearly uniform in intensity, indicating that the grains are randomly oriented. For deposition times as early as 6 min, the rings are nonuniform, indicating the development of preferred orientations. In Fig. 10, the ring intensity for the (111) ring is shown for various times. Up to 40 min there is considerable change in the profile. The change that occurs between 40 and 60 min is small, and there is almost no change after 60 min.

1. Grain size evolution

From the RHEED images, one can also see that the rings become sharper with increasing deposition time, and this suggests that the average grain size is increasing. For a one-dimensional crystal of size d, each diffraction spot has a profile with a full width at half maximum (FWHM) that is approximately given by[21]

$$\mathrm{FWHM} = \frac{2\pi}{d}. \tag{5}$$

For three-dimensional crystals, a given diffraction spot will be broadened in all three dimensions of reciprocal space. The degree of broadening in a given direction will depend on the size of the crystal in the corresponding real-space direction. Since the diffraction pattern for a polycrystalline film is merely the superposition of diffraction patterns from the individual crystals, broad diffraction spots for individual crystals will result in rings that are broadened in the radial direction. The broadening of a given ring will vary along the ring, because the radial direction varies along the ring and because the grain size and shape will vary with grain orientation. If the grain size and shape were the same for all grain orientations, then it would be reasonable to expect that the radial width l of a ring would follow

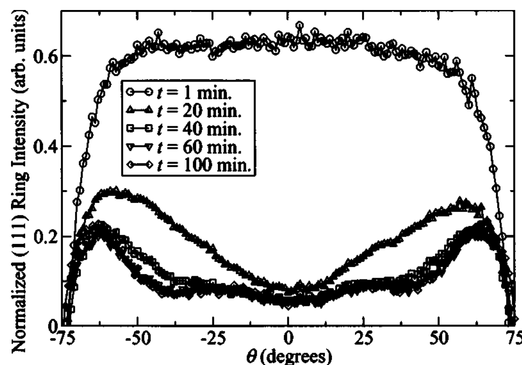

FIG. 10. Normalized ring intensity vs θ for the (111) ring at various times. Aside from $t=1$ min, each profile is the average of all profiles between 10 min earlier and 10 min later than the given time.

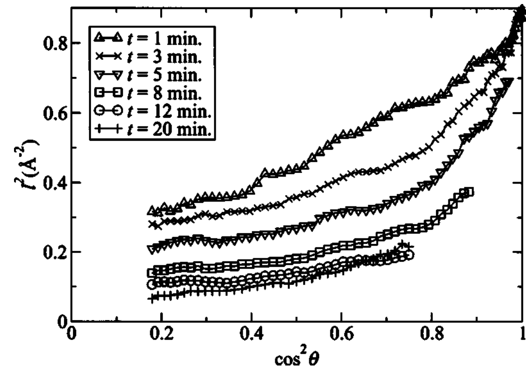

FIG. 11. l^2 vs $\cos^2\theta$, for the (111) ring, for various times.

$$l^2 = l_{\parallel}^2 \sin^2\theta + l_{\perp}^2 \cos^2\theta = l_{\parallel}^2(1-\cos^2\theta) + l_{\perp}^2 \cos^2\theta, \tag{6}$$

where $l_{\perp}$ is the radial width of the ring at $\theta=0°$ and $l_{\parallel}$ is the radial width of the ring at $\theta=90°$. In Fig. 11, $l^2(\theta)$, for the (111) ring, is plotted as a function of $\cos^2\theta$ for various times. For early times, the plot is reasonably close to a straight line over a wide range of angles, which indicates that the average grain size and shape are the same for nearly all grain orientations. For later times, though, the plot is a straight line over a smaller range of angles, indicating that some grain orientations are growing faster than others. The general trend, though, is for l to decrease with time, which implies that the grain sizes are increasing. Note, however, that l has increased, between $t=12$ min and $t=20$ min, for certain values of θ. This indicates that grains of certain orientations are actually shrinking.

In a manner analogous to Eq. (5), the grain width W and height H are inversely proportional to $l_{\parallel}$ and $l_{\perp}$, respectively. While the plot of l^2 versus $\cos^2\theta$ is not necessarily a straight line over the full range of angles, it should be close to a straight line over a limited range of angles, corresponding to the dominant grain orientations. Using this fact, the values of $l_{\parallel}$ and $l_{\perp}$ can be determined by using a straight line fit over this range of angles. Using this method, the grain width and height for the dominant grain orientations were computed, and the result is shown in Fig. 12. Not surprisingly, both the grain width and height increase with time. However, the grain height saturates at a value of ≈ 16 Å, after about 15 min. This does not mean that the grain height has stopped growing; it is simply a consequence of the fact that the electron beam cannot penetrate into the film more than about 16 Å. Thus, the electrons "see" a grain height of only 16 Å, even if the grain height is actually larger. After about 20 min, the grain width starts to fluctuate. This is a consequence of the fact that the level of noise in the RHEED images in-

Downloaded 21 Apr 2006 to 128.113.7.25. Redistribution subject to AIP license or copyright, see http://jap.aip.org/jap/copyright.jsp

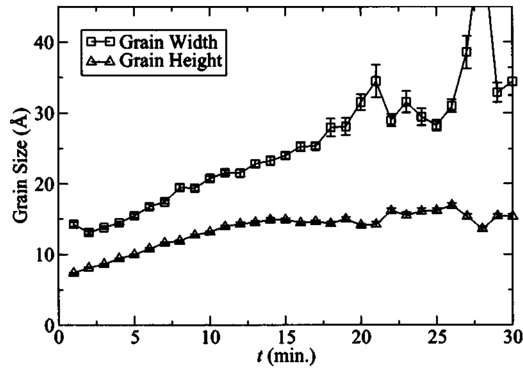

FIG. 12. Grain width and height vs time for the real-time copper deposition.

creases with time. It is also due to the shrinking range of angles over which the plot of l^2 versus $\cos^2\theta$ is a straight line.

To determine the grain width for longer times, a different approach was used. The value of $l_\perp$ was computed under the assumption that the grain height is 16 Å. The grain width could then be found, for various grain orientations, using Eqs. (5) and (6). This was done for two different grain orientations, and the results are shown in Fig. 13. Note that $l_\parallel$ was computed from an average of l^2 profiles between 5 min earlier and 5 min later than the given time. For both orientations, the grain width increases for early times. For $\theta = 45°-50°$, a peak occurs at 27 min, and a local minimum is reached at 63 min. For $\theta = 60°-65°$, there is a local minimum at 65 min. For both orientations, the grain width appears to level off near the end of the deposition.

2. Facet evolution

By looking at the specular reflection near the shadow edge, it is possible to obtain information on the surface of the film. It is expected that the surface consists of facets of various sizes and orientations. Individually, a facet is expected to be relatively flat. From Eq. (1), we know that a flat surface, in reciprocal space, will produce a narrow rod perpendicular to the surface. Since there are many facets of various orientations, reciprocal space will consist of a superposition of rods of various orientations. The result is a cone, in reciprocal space, whose apex is at the origin. Therefore the width,

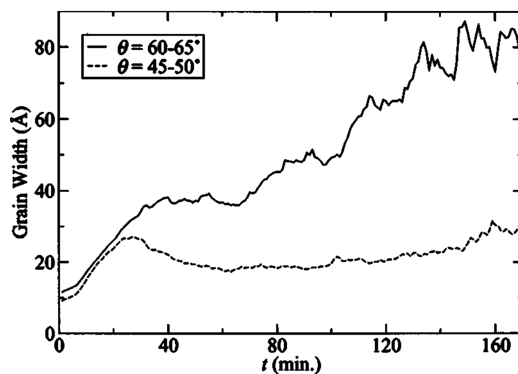

FIG. 13. Grain width vs time, for two different grain orientations, for the real-time copper deposition.

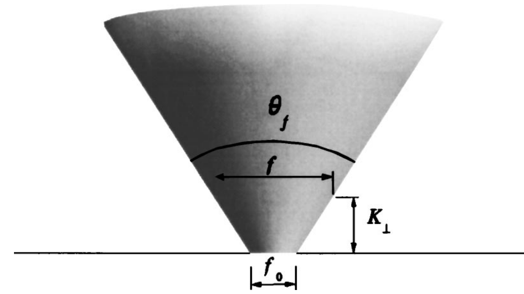

FIG. 14. The reciprocal-space structure for a surface consisting of finite-sized facets.

parallel to the shadow edge, of the specular reflection should increase with $K_\perp$. Specifically, we would expect this width f to satisfy

$$f = 2K_\perp \tan\frac{\theta_f}{2}, \tag{7}$$

where θ_f is the angular spread of facet orientations. However, this equation does not take into account the finite size of the facets. The effect of a finite facet size is to broaden the facet's reciprocal-space rod by an amount that is governed by Eq. (5). As a result, the reciprocal-space cone profile is convolved with the reciprocal-space rod profile. If we assume that both the cone and rod have Gaussian profiles parallel to the shadow edge, then f should actually obey

$$f^2 = f_0^2 + 4K_\perp^2 \tan^2\frac{\theta_f}{2}, \tag{8}$$

where f_0 is inversely proportional to the lateral facet size. The reciprocal-space structure for this type of situation is shown in Fig. 14. In Fig. 15, f^2 is plotted versus $K_\perp^2$ for various times. Each plot is an average of all profiles between 5 min earlier and 5 min later than the specified time. Each plot is close to a straight line, and the slope remains nearly constant over time. It was determined that $\theta_f = 29°$ over the entire course of film deposition, indicating that the facet normal vectors tend to be within 14.5° of the substrate normal vector. For times earlier than 50 min, f_0 is decreasing, indicating that the lateral facet size is increasing.

By making use of Eq. (1), it is also possible to determine, from the specular reflection, the average interface

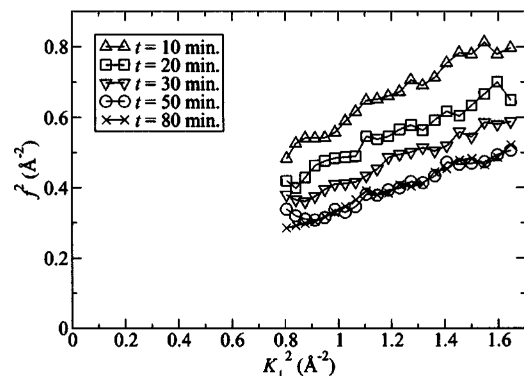

FIG. 15. f^2 vs $K_\perp^2$, for the specular reflection, for various times. Each profile is an average of all profiles between 5 min earlier and 5 min later than the specified time.

Downloaded 21 Apr 2006 to 128.113.7.25. Redistribution subject to AIP license or copyright, see http://jap.aip.org/jap/copyright.jsp

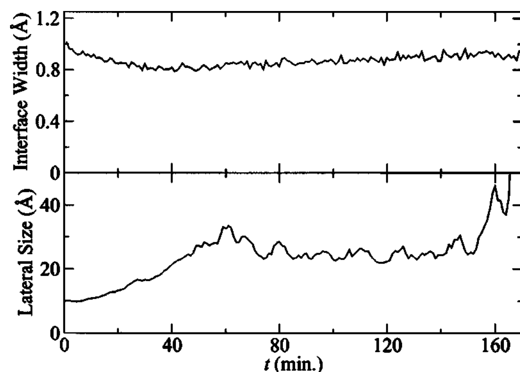

FIG. 16. The average interface width and lateral size, for individual facets, vs time for the real-time copper deposition.

width of the facets. Both the average interface width and lateral size of the facets are shown in Fig. 16. The interface width decreases and then increases, eventually flattening out towards the end of the deposition. The lateral facet size reaches a peak at 61 min, after which it decreases. Towards the end of the deposition, there is a sharp increase in the lateral facet size. However, due to increased noise, the facet size measurement is less reliable for later times.

IV. DISCUSSION

The work presented in this paper can be viewed from two different perspectives. First, it provides information on the mechanisms that are at work during the growth of copper films on silicon oxide substrates. It is also interesting from the perspective of film characterization since much of the diffraction analysis presented is different from conventional RHEED analysis.

A. Film characterization using RHEED

While RHEED has been used for decades to characterize the structure of crystalline substrates, its usefulness for characterizing polycrystalline substrates has only recently been realized. Several recent theoretical and experimental studies have demonstrated the use of RHEED for texture determination of polycrystalline films.[22–29] With the exception of the studies of Brewer *et al.*,[27–29] these studies have concentrated on the determination of grain orientations and have not attempted to extract quantitative information on grain sizes or shapes. Furthermore, no attempt has been made to analyze the specular reflection from the film; it is not even clear whether or not such a reflection was observed in these studies.

It is interesting to note that the specular reflection appears despite the fact that the electron beam penetrates a considerable distance into the film. The existence of this reflection can be attributed to scattering from the surface potential of the film; the electrons apparently experience a slightly higher scattering probability from the surface of the film than they experience from the bulk of the film.

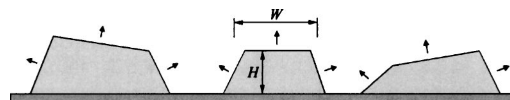

FIG. 17. Illustration of crystal growth. The grains grow in the directions indicated by the arrows. The grain width W and the grain height H, for the middle grain, are also indicated.

B. Polycrystalline film-growth mechanisms

A large amount of work has been devoted to understanding the growth mechanisms of polycrystalline films. Much of this work has been summarized by Barna and Adamik.[30] The growth of polycrystalline films can be divided into four stages: nucleation, crystal growth, coalescence, and thickness growth.[30] Nucleation is the process whereby the individual crystals are formed; a deposited atom diffuses over the substrate until contacting another deposited atom or an existing crystal. Nucleation occurs at random positions on the substrate, but the crystal orientations are not necessarily random. In the case of the real-time copper deposition, however, the initial crystal orientations are random. This follows from the fact that the normalized ring intensity is nearly constant at early times, as is seen in Fig. 10.

Following the nucleation stage, the individual crystals (grains) grow by incorporating deposited atoms. This is illustrated in Fig. 17. For such a case, it is expected that the grain volume would undergo a linear increase, since atoms are incorporated into the grains at a constant rate. In Fig. 18, the grain volume, as computed from the grain width and height, is shown as a function of time, for early times. The aspect ratio, defined as the ratio of the grain width to the grain height, is also shown. Between 3 and 15 min, the grain volume increases linearly with time, and the aspect ratio is nearly constant at a value of 1.6. Note that the volume and aspect ratio calculations are probably not valid after 15 min, because the finite electron penetration depth makes it impossible to measure the grain height. Prior to 3 min, the grain volume is nearly constant. This is due to nucleation; the formation of new grains keeps the average grain volume from increasing.

As crystal growth continues, the individual grains will eventually coalesce, and when this happens, a grain boundary is formed. After coalescence is completed, grains con-

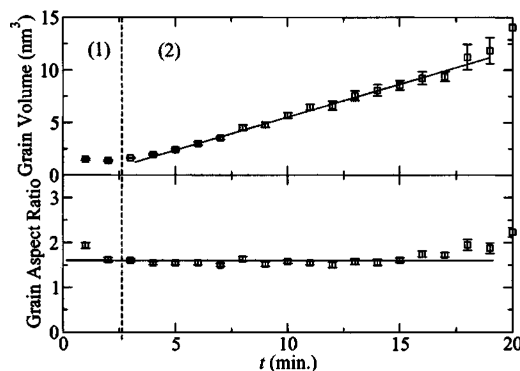

FIG. 18. Grain volume and grain aspect ratio vs time for the real-time copper deposition. The dashed line divides the plots into two regimes: (1) nucleation and (2) grain growth.

Downloaded 21 Apr 2006 to 128.113.7.25. Redistribution subject to AIP license or copyright, see http://jap.aip.org/jap/copyright.jsp

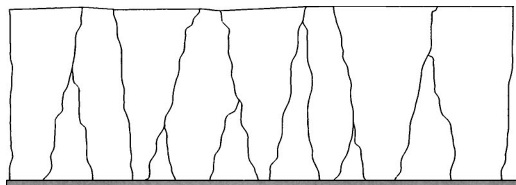

FIG. 19. Illustration of competitive texture evolution. Grains with high adatom binding energy grow at the expense of those with lower adatom binding energy.

tinue to grow vertically at their exposed faces. Grains can grow laterally by either grain boundary migration or competitive texture growth. Competitive texture growth requires a high adatom mobility; a deposited atom will move around on the surface until it is incorporated into a grain. Competition arises, because some crystal faces have higher adatom mobility than others. Using a kinetic Monte Carlo simulation, Smith found that, in such a situation, grains that have high adatom binding energies (and, hence, low adatom mobilities) tend to become larger at the expense of grains with lower adatom binding energies.[31,32] This is illustrated in Fig. 19. The adatom binding energy for a given crystal face will depend on the number of nearest neighbors (and, possibly, the number of next-nearest neighbors) that an adatom has. For two crystal faces, it will be assumed that the face with the highest adatom binding energy is the face where adatoms have the highest number of nearest neighbors. If, for two crystal faces, adatoms have the same number of nearest neighbors, it will be assumed that the face with the highest adatom binding energy is the face where adatoms have the highest number of next-nearest neighbors. For fcc lattices, adatoms on the (111), (200), (220), (113), (133), and (420) crystal faces will have 3, 4, 5, 5, 5, and 6 nearest neighbors, respectively. The adatoms on these faces have 3, 1, 2, 3, 3, and 2 next-nearest neighbors, respectively. Thus, it is not surprising that we see an absence of (111), (200), and (220) texture, because these crystal faces have lower adatom binding energies than the (113) and (331) faces. In Fig. 13, it is seen that some grains begin to shrink after 27 min of growth time. This is probably the point where coalescence is completed; after this point, only grains with high adatom binding energy can continue to grow.

Compared to the grain evolution, the evolution of facets is more difficult to explain. One might naively expect that the facet size should follow the same trend as the grain size. However, this presumes that the number of facets per grain is constant. The measured lateral facet size is shown, in semilogarithmic scale, in Fig. 20. Aside from the earliest and latest times, and aside from an anomaly near $t=27$ min (the point where coalescence becomes complete), the plot is close to a straight line indicating that the facet size is increasing exponentially. For early times, the facet size is smaller than the grain size indicating that at least some grains contain multiple facets. Eventually, the number of facets per grain decreases. The trend in the lateral facet size can be explained in terms of facet coalescence; when facets coalesce, the facet area increases by an amount proportional to the facet area. If the rate of coalescence is constant, then the facet area will grow exponentially with time, which implies an exponential

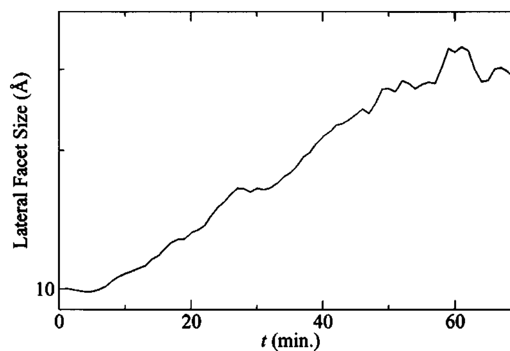

FIG. 20. Lateral facet size vs time, in semilogarithmic scale, for the real-time copper deposition.

increase in facet size. It should be pointed out that, for two facets to coalesce, the facets must be parallel to begin with. Thus, for this idea to make sense, most of the facets of an individual grain must have the same orientation. Taking this into account, it becomes clear that the lateral facet size cannot grow beyond the grain size, which could explain why the exponential increase eventually stops.

V. CONCLUSION

The real-time deposition study presented here indicates that the growth of copper on silicon oxide is governed, after coalescence, by competitive texture evolution, where grains having crystal faces with high adatom binding energies grow at the expense of grains with lower adatom binding energies. In addition, analysis of the facet growth suggests that the growing crystals initially contain facets that grow exponentially due to coalescence.

The diffraction analysis presented here has also revealed interesting capabilities of RHEED, such as the ability to determine the interface width and lateral size of facets from a specular reflection and the ability to extract both the grain width and grain height from a polycrystalline ring pattern. The work presented here should further demonstrate the usefulness of RHEED for real-time monitoring of polycrystalline film growth.

ACKNOWLEDGMENTS

This work was supported by the NSF. We thank H. Huang, F. Tang, and T. Karabacak for invaluable discussions. We thank F. Tang for performing the temperature measurements.

[1] C.-A. Chang, J. Appl. Phys. **67**, 566 (1990).
[2] L. Stolt and F. M. D'Heurle, Thin Solid Films **189**, 269 (1990).
[3] A. Cros, M. O. Aboelfotoh, and K. N. Tu, J. Appl. Phys. **67**, 3328 (1990).
[4] R. Padiyath, J. Seth, S. V. Babu, and L. J. Matienzo, J. Appl. Phys. **73**, 2326 (1993).
[5] C. S. Liu and L. J. Chen, J. Appl. Phys. **74**, 5501 (1993).
[6] I. Hashim, B. Park, and H. A. Atwater, Appl. Phys. Lett. **63**, 2833 (1993).
[7] C. S. Liu and L. J. Chen, Appl. Surf. Sci. **92**, 84 (1996).
[8] S. Iida, T. Shindo, S. Matsuura, and Y. Ashimura, Nucl. Instrum. Methods Phys. Res. B **121**, 162 (1997).
[9] T. Yasue and T. Koshikawa, Surf. Sci. **377**, 923 (1997).
[10] N. Benouattas, A. Mosser, and A. Bouabellou, Mater. Sci. Eng., A **288**, 253 (2000).
[11] N. Benouattas, A. Mosser, D. Raiser, J. Faerber, and A. Bouabellou, Appl. Surf. Sci. **153**, 79 (2000).

Downloaded 21 Apr 2006 to 128.113.7.25. Redistribution subject to AIP license or copyright, see http://jap.aip.org/jap/copyright.jsp

[12]J. S. Jeng and J. S. Chen, J. Electrochem. Soc. **148**, G232 (2001).
[13]F. M. Reicha, M. E. Hiti, and P. B. Barna, Vacuum **37**, 93 (1987).
[14]H. L. Wei, H. Huang, C. H. Woo, R. K. Zheng, G. H. Wen, and X. X. Zhang, Appl. Phys. Lett. **80**, 2290 (2002).
[15]M. Grundner and H. Jacob, Appl. Phys. A: Solids Surf. **39**, 73 (1986).
[16]W. Kern and D. A. Puotinen, RCA Rev. **31**, 187 (1970).
[17]L. E. Davis, N. C. MacDonald, P. W. Palmberg, G. E. Riach, and R. E. Weber, *Handbook of Auger Electron Spectroscopy*, 2nd ed. (Physical Electronics Division, Perkin-Elmer Corp., 1976).
[18]Y.-P. Zhao, G.-C. Wang, and T.-M. Lu, *Characterization of Amorphous and Crystalline Rough Surface: Principles and Applications* (Academic, New York, 2001).
[19]Y.-P. Zhao, G.-C. Wang, and T.-M. Lu, Phys. Rev. B **55**, 13938 (1997).
[20]M. P. Seah and W. A. Dench, Surf. Interface Anal. **1**, 2 (1979).
[21]H.-N. Yang, G.-C. Wang, and T.-M. Lu, *Diffraction from Rough Surfaces and Dynamic Growth Fronts* (World Scientific, Singapore, 1993).
[22]S. Andrieu and P. Fréchard, Surf. Sci. **360**, 289 (1996).
[23]D. Litvinov, T. O'Donnell, and R. Clarke, J. Appl. Phys. **85**, 2151 (1999).
[24]D. Litvinov and R. Clarke, Appl. Phys. Lett. **74**, 955 (1999).
[25]D. Litvinov, J. K. Howard, S. Khizroev, H. Gong, and D. Lambeth, J. Appl. Phys. **87**, 5693 (2000).
[26]T. Kitagawa, M. Kondo, and A. Matsuda, J. Non-Cryst. Solids **266**, 64 (2000).
[27]R. T. Brewer, J. W. Hartman, and H. A. Atwater, Mater. Res. Soc. Symp. Proc. **585**, 75 (2000).
[28]R. T. Brewer, J. R. Groves, P. N. Arendt, P. C. Yashar, and H. A. Atwater, Appl. Surf. Sci. **175–176**, 691 (2001).
[29]R. T. Brewer, P. N. Arendt, J. R. Groves, and H. A. Atwater, Proc. SPIE **4468**, 124 (2001).
[30]P. B. Barna and M. Adamik, in *Science and Technology of Thin Films*, edited by F. C. Matacotta and G. Ottaviani (World Scientific, Singapore, 1995), p. 1.
[31]R. W. Smith, J. Appl. Phys. **81**, 1196 (1997).
[32]F. H. Baumann, D. L. Chopp, T. D. de la Rubia, G. H. Gilmer, J. E. Greene, H. Huang, S. Kodambaka, P. O'Sullivan, and I. Petrov, MRS Bull. **26**, 182 (2001).

Downloaded 21 Apr 2006 to 128.113.7.25. Redistribution subject to AIP license or copyright, see http://jap.aip.org/jap/copyright.jsp